Ore Geology Reviews 86 (2017) 624–638

Contents lists available at ScienceDirect

Ore Geology Reviews

journal homepage: www.elsevier.com/locate/oregeo

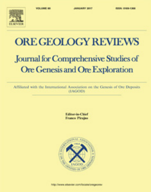

Ore fluid evolution in the giant Marcona Fe-(Cu) deposit, Perú: Evidence from in-situ sulfur isotope and trace element geochemistry of sulfides

Rucao Li [a,b], Huayong Chen [c,d,*], Xiaoping Xia [a,*], Qing Yang [a], Ling Li [a,b], Jian Xu [a,b], Chao Huang [a,b], Leonid V. Danyushevsky [e]

[a] *State Key Laboratory of Isotope Geochemistry, Guangzhou Institute of Geochemistry, University of Chinese Academy of Sciences, Guangzhou 510604, China*
[b] *Graduate University of Chinese Academy of Sciences, Beijing 100049, China*
[c] *Key Laboratory of Mineralogy and Metallogeny, Guangzhou Institute of Geochemistry, Chinese Academy of Sciences, Guangzhou 510604, China*
[d] *State Key Laboratory of Ore Deposit Geochemistry, Institute of Geochemistry, Chinese Academy of Sciences, Guiyang 550002, China*
[e] *ARC Centre for Excellence in Ore Deposits (CODES), University of Tasmania, Hobart 7001, Australia*

ARTICLE INFO

Article history:
Received 30 November 2016
Received in revised form 17 March 2017
Accepted 20 March 2017
Available online 30 March 2017

Keywords:
Marcona Fe-(Cu) deposit
IOCG
Sulfide trace element
Sulfur isotopes
Perú

ABSTRACT

The Marcona magnetite deposit, located in the iron oxide copper-gold (IOCG) province of southern Perú, is an important Fe deposit with sub-economic Cu and Zn mineralization. Three generations of sulfides were identified at the Marcona alteration/mineralization Stages IV, V and VII. Magnetite, pyrrhotite, pyrite and minor chalcopyrite started to form at Stage IV. Sulfides in Stage V are dominated by chalcopyrite and pyrite, whereas only pyrite was present in Stage VII. In-situ SIMS sulfur isotope and LA-ICP-MS trace element analyses were conducted on the sulfides of these stages. Stage IV sulfides contain $\delta^{34}S$ largely in the range of 0 to +4.0‰, indicating a dominantly magmatic origin. In particular, $\delta^{34}S$ values of Stage IV pyrite increase from core to rim, and the corresponding trace elements concentrations vary along with $\delta^{34}S$. Positive $\delta^{34}S$ vs. Se/S correlation of Stage IV pyrite indicates that the ore-forming system was open. The Stage V pyrite are rich in Mn, Cu, Ag, Sb, Te, Pb and Bi, and all Stage V sulfides have also elevated $\delta^{34}S$ (up to +7.8‰), indicative of possible seawater incursion during its formation. The $\delta^{34}S$ values of Stage VII pyrite are highly variable from −13.4 to 5.4‰. This, together with ubiquitous disseminated voids, low Co/Ni ratios and enrichments of Mn, Se, Sb, Te, Tl and Pb, suggests that Stage VII pyrite may have formed by sulfate reduction associated with organic materials. We propose that the ore-forming fluids of Stage IV are initially magmatic with involvement of external (e.g., seawater) at late, where the fluids of Stage V are likely mainly exotic. The external fluids, together with organic matter, may have contributed to the ore-forming fluids of Stage VII, indicating a complex fluid evolution history for this giant Fe (-Cu) deposit.

1. Introduction

The iron oxide copper-gold (IOCG) deposit clan was proposed more than twenty years ago (Hitzman et al., 1992) and remains controversial since then, particularly in terms of its nature, metal/fluid source and interrelations of ore-forming fluids. Previous studies have shown that the IOCG ore-forming fluids were mainly magmatic-hydrothermal (Baker et al., 2001; Marschik and Fontbote, 2001; Sillitoe, 2003; Oliver et al., 2004; Pollard, 2006; Groves et al., 2010), yet non-magmatic fluids (e.g., seawater and basinal fluids) were also recognized, especially for the late Cu-(Au) mineralization stage (Benavidies et al., 2007; Chen et al., 2011; McPhie et al., 2011). Furthermore, fluid-mixing was proposed for those deposits where multiple hydrothermal fluids were identified (Haynes et al., 1995; Williams et al., 2001; Oliver et al., 2004). Elucidating the fluid sources and their contribution to ore formation would allow better IOCG ore deposit modeling and hence exploration targeting.

The Marcona deposit lies in the iron oxide copper-gold (IOCG) province of southern Perú. This deposit is hosted by the Paleozoic metasedimentary and Jurassic andesitic and sedimentary rocks, and has a reserve of 1551 Mt ore @ 55.4% Fe and 0.12% Cu (Chen et al., 2010a). The Mina Justa Cu-(Ag) deposit, the largest IOCG deposit so far discovered in Perú, is located at about 3.5 km northeast of Marcona (Chen et al., 2010a). Hudson (1974) suggested that the Marcona deposit is a partially remobilized Paleozoic sedimentary ironstone deposit, whereas other researchers (Atchley, 1956; Atkin et al.,

---

[*] Corresponding authors at: Key Laboratory of Mineralogy and Metallogeny, Guangzhou Institute of Geochemistry, Chinese Academy of Sciences, Guangzhou 510640, China (H. Chen).

E-mail addresses: huayongchen@gig.ac.cn (H. Chen), xpxia@gig.ac.cn (X. Xia).

http://dx.doi.org/10.1016/j.oregeorev.2017.03.025

1985; Injoque, 1985) suggested that Marcona is an epigenetic replacement-type skarn deposit. Afterwards, Injoque (2002) and Hawkes et al. (2002) classified it as an IOCG deposit, and Chen et al. (2010a, 2011) further proposed that the Marcona mineralization was a product of a hydrous, iron oxide-rich melt, with the sulfides being precipitated in a fluid system with seawater involvement.

Several in-situ isotope and trace element study were applied on different minerals (e.g., apatite: Zhao et al., 2015; magnetite: W.T. Chen et al., 2015a,b; titanite: Storey and Smith, 2016) to constrain source of metal and ore fluids and their evolution. However, only a few in-situ sulfur isotope and trace elements analysis have been applied on sulfides of Marcona deposit and other "sensu stricto" IOCG deposits (Case et al., 2015a,b). Sulfur isotopes have long been used to trace the source of ore-forming fluids (Ohmoto, 1972; Rye and Ohmoto, 1974; Seal, 2006), but traditional bulk grain analysis cannot reveal possible variation of sulfur isotope composition in individual sulfide grains, especially for those deposits like Marcona, in which the pyrite is usually coarse-grained (up to 6 mm) and Cu (-Zn) sulfides formed later than pyrite (Chen et al., 2010b). Besides, LA-ICP-MS sulfide trace element geochemistry is a powerful tool for constraining the fluid evolution process, ore-forming fluid source and metallogenic environment (Maslennikov et al., 2009; Scott et al., 2009; Thomas et al., 2011; Zheng et al., 2013; W.T. Chen et al., 2015a,b). In this study, we present new in-situ sulfur isotope and trace element data of the Marcona sulfides (of Stage IV, V and VII). With the new data, we discuss the source and ore-forming fluids (esp. for the sulfide-bearing stages) and sulfide genesis, as well as the possible genetic link with nearby large-size Mina Justa IOCG deposit.

2. Regional and ore deposit geology

The basement of the IOCG belt in southern Perú consists of Paleo-to-Mesoproterozoic high-grade metamorphic rocks of the Arequipa Massif, which comprises gneiss, granites, migmatite and schist (Wasteneys et al., 1995; Loewy et al., 2004). Overlying the basement is the Neoproterozoic San Juan Formation and Paleozoic Marcona Formation sedimentary cover (Caldas Vidal, 1978; Hawkes et al., 2002). The Marcona Formation (1500 m thick) contains conglomerate-sandstone-siltstone, dolomitic marble and silicified limestones, and host most of the Marcona magnetite orebodies. The Marcona Formation is overlain by a thick Mesozoic meta-sedimentary/volcanic succession, which comprise

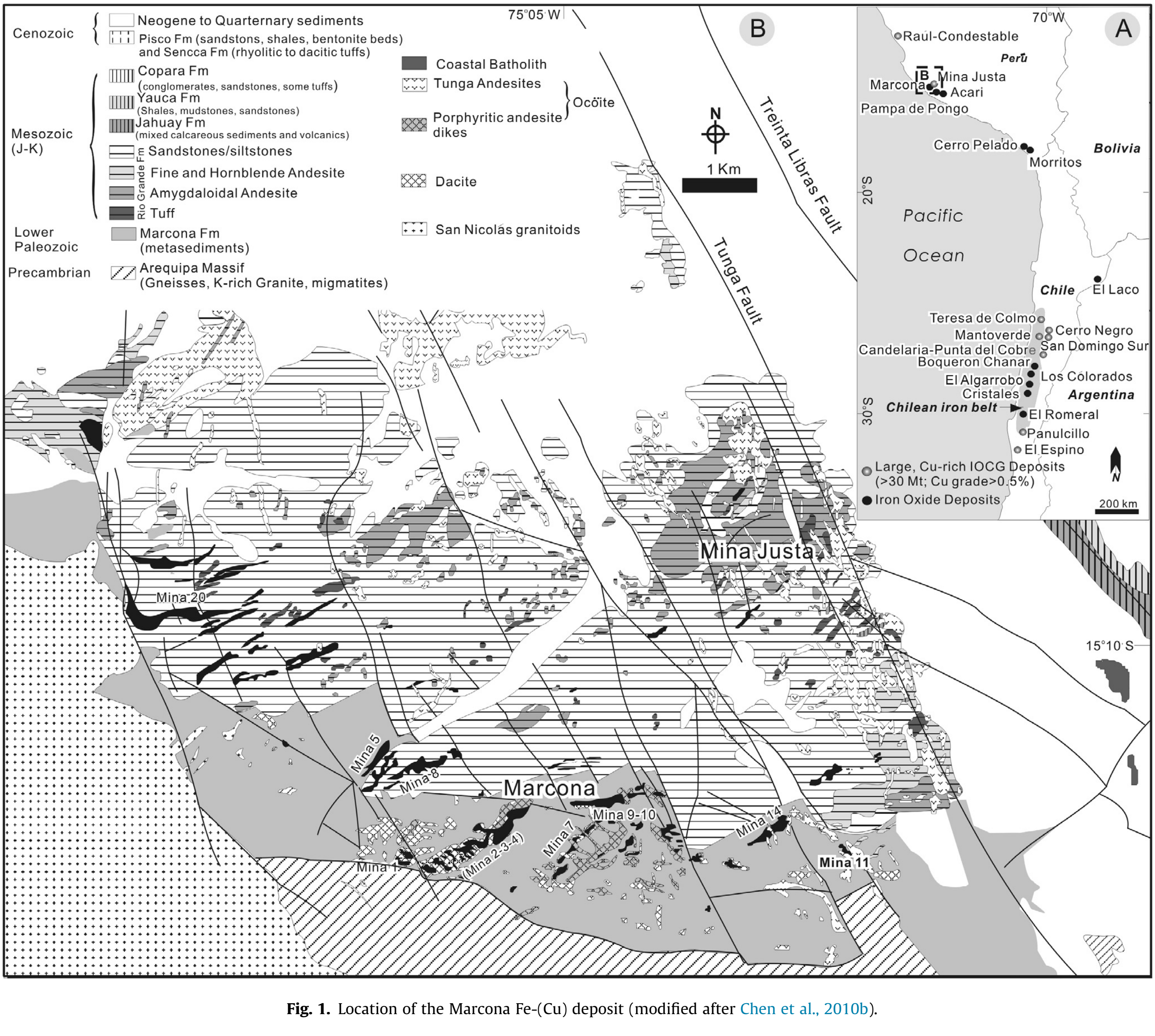

Fig. 1. Location of the Marcona Fe-(Cu) deposit (modified after Chen et al., 2010b).

(from bottom to top) the Río Grande, Jahuay, Yauca and Copara formations (Caldas Vidal, 1978). The Mesozoic and older rocks are overlain discordantly by a Tertiary sequence, which can be subdivided into, from bottom to top, the Pisco, Millo and Sencca formations.

A series of latest Triassic to Holocene volcano-plutonic arcs are exposed in the southern-central Perú cordillera, testifying to multiphase supra-subduction magmatism along the western margin of South America. Multistage magmatism is also observed in the Marona-Mina Justa district. The oldest igneous event is represented by the ca. 425 ± 4 Ma San Nicolás batholith that consisted of monzogranites, granodiorites and gabbro-diorites which intruded the Marcona Formation and San Juan Formation (Fig. 1) (Mukasa and Henry, 1990; Vidal et al., 1990). The Mesozoic igneous activity is recorded by the emplacement of the Bella Unión complex, dominantly consisting of hypabyssal andesite and dacite, and it intruded the Copara Formation and older unites. The age of this magmatism is poorly constrained, but according to stratigraphic relation, the emplacement of the Bella Unión complex should be around 109 ± 4 Ma (Cobbing, 1999; Chen et al., 2010b). The next igneous event is recorded by the emplacement of the Tunga Andesite (Caldas Vidal, 1978), whose most characteristic lithology is a rock with large glomerocrysts of labradorite and sparse augite phenocrysts. This magmatism is characterized by dike swarms, sills and small plugs, and its age is also poorly defined. Constrained by $^{40}Ar/^{39}Ar$ biotite plateau age of rhyodacitic ash-flow tuff in this district, the Tertiary igneous event occurred at about 9.13 ± 0.25 Ma (2σ) (Quang et al., 2005).

Four major fault systems were identified at Marcona (Fig. 1; Hawkes et al., 2002; Chen et al., 2010b). The Pista normal faults strike ~ 295° and dip ~ 60° to the north. Together with the coeval or younger Repetición faults, they were interpreted to have formed during the Jurassic compressive tectonics (Hawkes et al., 2002). The Mina Justa faults, which control the main magnetite bodies at Marcona and Cu mineralization at Mina Justa, have strike directions similar to the Repetición faults. The Juaca normal faults are post-mineralization at both Marcona and Mina Justa, and they are commonly followed by porphyritic andesitic dikes (Chen et al., 2010b).

Most of the ore resource at Marcona deposit is hosted by the Marcona Formation, and the rest by the lower members of the Río Grande Formation (Chen et al., 2010b). The dominant ore mineral (>90%) is massive magnetite, and most original contacts between the orebodies and the Paleozoic and Jurassic host rocks are abrupt, only locally complicated by minor stockwork veining, hydrothermal breccias and disseminated mineralization. Total sulfide mineral contents and Cu grades are elevated in the upper part of orebodies, and the orebodies are locally dissected by post-mineralization faults (Chen et al., 2010a).

2.1. Paragenesis

Seven hydrothermal alteration-mineralization stages (labelled I to VII) have been recognized at Marcona (Fig. 2; Chen et al., 2010a and this study).

The fine-grained cummingtonite aggregates are assigned to paragenetic Stage IA. This alteration is restricted to the envelopes of orebodies in the upper Marcona Formation, and is locally replaced by biotite and magnetite. The coarse-grained phlogopite, together with magnetite, is assigned to Stage IB. The Na-Cl metasomatism which generated massive albite and subordinate Na-rich scapolite is assigned to Stage II. This alteration mainly occurs

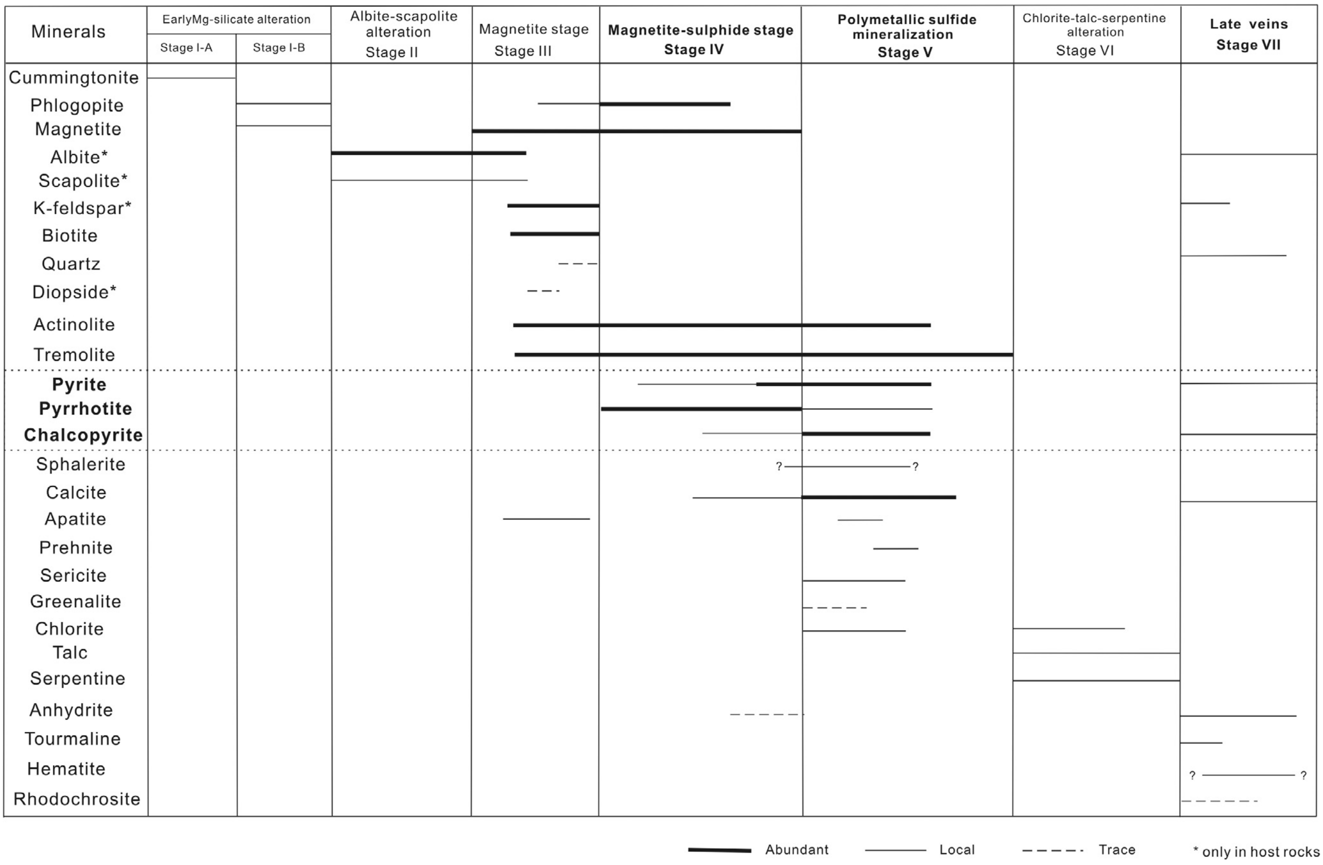

Fig. 2. Alteration and mineralization paragenesis of the Marcona Fe-(Cu) deposit (modified after Chen et al., 2010b).

in Marcona Formation siliciclastics and lower Río Grande Formation sedimentary units and andesites. The coarse white albite and scapolite are developed widely along the foliation of host rocks, in places adjacent to massive magnetite bodies. But albite and scapolite do not occur within the massive magnetite bodies. Predating magnetite mineralization, much of this alteration is assigned to Stage II. Na-rich scapolite is locally replaced by amphibole and magnetite. The Stage III (magnetite) and IV (magnetite-sulfide) mineralization constitute >95% of the magnetite mineralization. The dominant Stage III metallic mineral is magnetite, whereas gangue minerals include phlogopite, K-feldspar, biotite, actinolite, tremolite and minor apatite. Major Stage IV sulfides include pyrrhotite, pyrite and minor chalcopyrite, while gangue minerals include phlogopite, actinolite, tremolite and calcite (Fig. 3A, B). In both Stage III and Stage IV, magnetite mainly occurs as euhedral to subhedral, 0.3–5 mm grains and as aggregates, and usually intergrown with light-green tremolite or dark-green actinolite. Stage III biotite and K-feldspar alteration usually occur in dacite and fine-grained andesite, and biotitization usually gave away outwards to K-feldspar and albitic alteration (with or without magnetite). The major Stage IV sulfides usually occur as subhedral to anhedral crystals interstitial to magnetite (Fig. 3B), calcic amphibole and phlogopite. Local biotite and phlogopite were found in hanging wall and footwall Marcona Formation metasediments. Accessory minerals include fine-grained Stage III fluorapatite and Stage IV calcite. Magnetite is absent at Stage V, and the main opaque minerals are pyrite and chalcopyrite, with gangue minerals of calcite, chlorite, actinolite and tremolite. Stage V sulfide veins, commonly with calcic amphiboles (Fig. 3C), crosscut Stage III and Stage IV magnetite-amphibole associations in the upper parts of the orebodies (Fig. 3C). Pyrite, chalcopyrite and calcite at this stage commonly occur as aggregates in cavities (Fig. 3D), replacing Stage III magnetite-amphibole (Fig. 3D). Stage V sulfides usually occur as euhedral to subhedral grain, and they commonly have planar contacts with calcite (Fig. 3D), indicating coeval precipitation. Stage VI alteration minerals (e.g., chlorite, talc and serpentine) are considered to be the result of retrograde alteration of calcic amphiboles, which indicates Mg metasomatism following Stage V sulfide precipitation. In this stage, talc, commonly as fine-grained aggregates, replaces and cuts calcite, while serpentine, locally talc, replaces Stage V actinolite and tremolite.

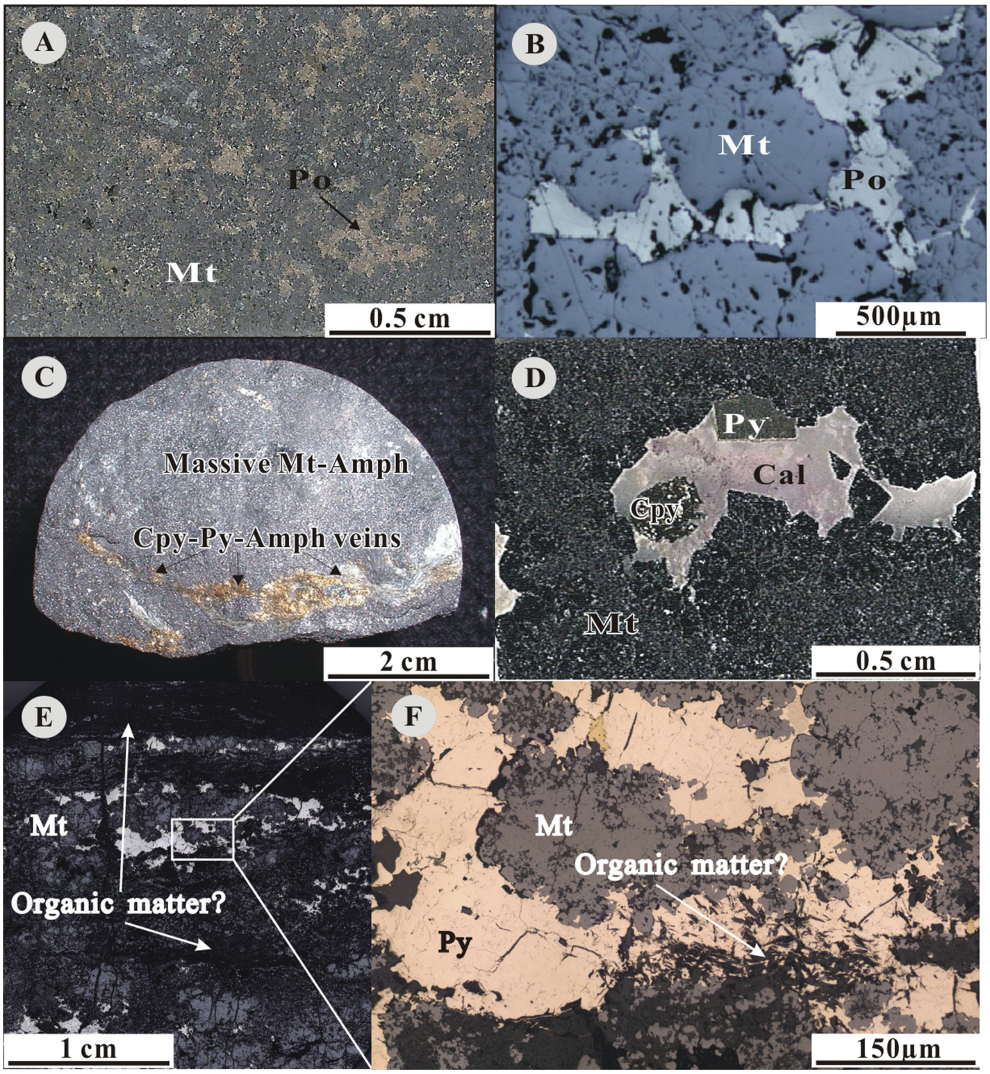

Fig. 3. Photographs and photomicrographs of the Marcona Fe-(Cu) ores: (A) and (B) Coexisting Stage IV magnetite and pyrrhotite (DDM4-6-225). (C) Stage V chalcopyrite-pyrite-tremolite-actinolite veins crosscut Stage III massive magnetite-amphibole aggregates (DDM5-4-2). (D) Stage V chalcopyrite-pyrite-calcite aggregates overprinting Stage III magnetite (MA5-3). (E) and (F) Stage VII pyrite crosscut Stage III magnetite (DDM4-6-160). Abbreviations: Mt: magnetite. Py: pyrite. Cpy: chalcopyrite. Po: pyrrhotite. Cal: calcite. Amph: amphibole.

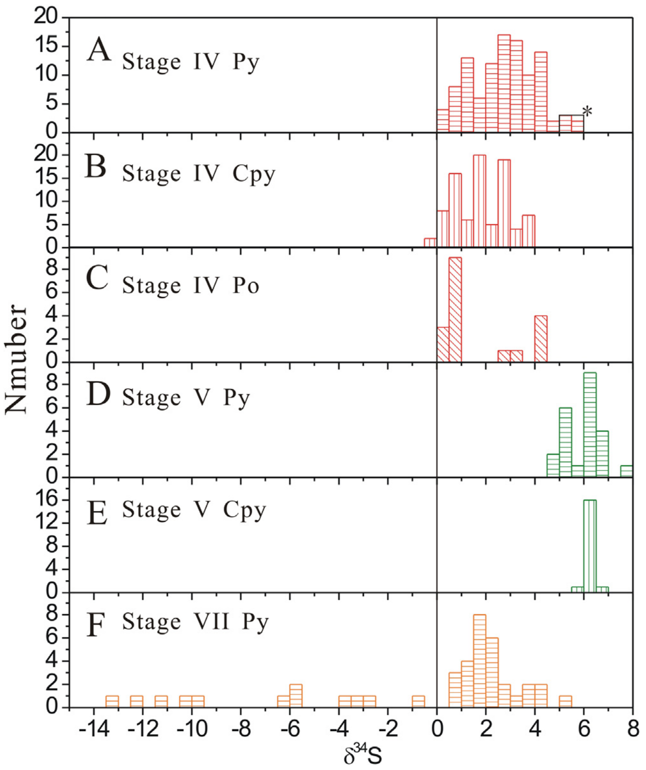

Fig. 4. In-situ $\delta^{34}S$ histogram of the Marcona sulfides. (A): Stage IV pyrite. The histogram with "*" may belong to Stage V. (B): Stage IV chalcopyrite. (C): Stage IV pyrrhotite. (D): Stage V pyrite. (E): Stage V chalcopyrite. (F): Stage VII pyrite.

Stage VII alteration minerals include tourmaline, quartz, pyrite, and hematite, which commonly occur as veins crosscutting previous alteration stages and replacing early-stage magnetite (Fig. 3E, F).

3. Sampling and analytical techniques

3.1. In-situ SIMS sulfur isotope analysis

This SIMS analysis was conducted with a Cameca IMS1280-HR at the Guangzhou Institute of Geochemistry, Chinese Academy of Sciences (GIGCAS). A total of 278 spots on 21 sulfide samples of Stage IV (n = 17), Stage V (n = 3) and Stage VII (n = 2) were analyzed. Analytical procedures were summarized as follows:

The samples were cut into small pieces and mounted into 25 mm diameter epoxy. The mounted samples were carefully polished and micro photos were collected under microscope with reflected light in order to locate the analysis spot. A primary $^{133}Cs^{+}$ ion beam (~2.0 nA) and a total impact energy of 20 keV were used with a spot size of ~15 µm diameter. 20 s presputtering was applied to remove the Au coating, and a normal-incidence electron gun is utilized for charge compensation. The mass resolving power was set at ~5000 to avoid isobaric interference. ^{32}S, ^{33}S and ^{34}S were collected simultaneously by the multicollection system. The total analysis time for one spot was about 4 min. Data reduction was as outlined in Ushikubo et al. (2014), and the primary standards used in this study were PPP-1 (Gilbert et al., 2014) for pyrite, CPY-1 (in-house standard) for chalcopyrite, and Polo (in-house standard) for pyrrhotite (Molnár et al., 2016). Py-1 (Molnár et al., 2016) was used as secondary standards in order to monitor the reliability of the whole analytical procedure.

3.2. In-situ LA-ICP-MS trace element and EMPA analyses

A total of 60 spots of eight sulfide samples (pyrite, chalcopyrite and pyrrhotite) of Stages IV (n = 5), V (n = 2) and VII (n = 1) were analyzed with LA-ICP-MS. Before the LA-ICP-MS analysis, detailed petrographic observation and EPMA analyses were performed to reveal any morphological and/or isotopic heterogeneity within each sulfide grain. The EMPA analysis was performed with a JXA-8230 electron microprobe at the Guangzhou Institute of Geochemistry, Chinese Academy of Sciences (GIGCAS), with an accelerating voltage of 20 kV, beam current of 20 nA and electron beam of 3 µm diameter. The LA-ICP-MS analysis was conducted at CODES (ARC Centre of Excellence in Ore Deposits, Tasmania, Australia) using a New Wave 213-nm solid-state laser microprobe coupled with an Agilent 7500 Quadrupole ICP-MS. Detailed analysis parameters were described in Large et al. (2007, 2009) and were summarized below:

Analytical spot size: 50 µm (diameter); Laser repetition rate: 5 Hz; Beam energy: 7.2 J/cm^2. Analysis time: 90 s/spot, including 30 s background measurement with laser off and 60 s sample analysis with laser on. A total of 37 elements were analyzed.

Data reduction was conducted using the internal standard method (Longerich et al., 1996), and Fe was used as the internal standard. STDGL2b2 was used as the primary calibration standard (Danyushevsky et al., 2011), which was analyzed with a 100 µm beam at 10 Hz twice every 1.5 h to monitor any instrumental drift.

4. Results

4.1. In-situ SIMS sulfur isotopes

4.1.1. Stage IV: magnetite-sulfide mineralization

The pyrite of this stage has $\delta^{34}S$ values of +0.2‰ to +5.8‰, and show distinct normal distribution with mode occurring at about +3.0‰ (Fig. 4A). When individual sulfide grain is considered, the pyrite $\delta^{34}S$ is usually homogeneous, with the intra-grain variation usually <1‰ (Fig. 5A). Two exceptions are Sample DDM3-3-418, whose core is quite homogeneous (+3.0‰) and surrounded by rim with elevated $\delta^{34}S$ value (+4.8‰) (Fig. 5B), and Sample DDM-22-268, which has its $\delta^{34}S$ increase gradually from +2.3‰ in the core to +6.0‰ in the rim (Fig. 5C). A zonation texture was evident in wavelength dispersive spectrometry (WDS) and LA-ICP-MS mapping (Figs. 6 and 8) of both samples. In both samples, the pyrite occurs as subhedral to euhedral, 0.3–6 mm grains, while magnetite as subhedral to euhedral massive aggregates. Pyrite and magnetite commonly have planar contacts, indicating broadly coeval precipitation, but locally pyrite occurs as veinlets cutting massive magnetite aggregates. Many pyrite grains have a distinct zoning structure, which usually has a core free of mineral inclusions, an inner rim full of amphibole inclusions, and an inclusion-free outer rim (Fig. 5B). Additionally, together with massive amphibole inclusions, many magnetite inclusions are presented in the inner rim of the pyrite. Based on microscopy observation, in-situ sulfur isotope, WDS and LA-ICP-MS mapping, we suggest that the core and inner rim of the pyrite, together with magnetite and amphibole, belong to Stage IV, while the outer rim of the pyrite belongs to Stage V. The $\delta^{34}S$ values of Stage IV chalcopyrite are of −0.2‰ to +4.0‰ (mainly +1 to +3‰) (Fig. 4B), which are slightly lower than those of Stage IV pyrite (Fig. 4A, B), a feature typically found for the chalcopyrite and pyrite that formed together (Bachinski, 1969; Kajiwara and Krouse, 1971). The $\delta^{34}S$ values of Stage IV pyrrhotite range from +0.3‰ to +4.3‰, similar with their pyrite and chalcopyrite counterparts (Fig. 4C). The rims of both Sample DDM3-3-418 and DDM-22-268 have $\delta^{34}S$ values of +4.3 to +6.0‰, which are similar with samples of Stage V (Fig. 5D, E) and higher than samples of Stage IV

(Fig. 5B, C) and Stage VII (Fig. 5G). Besides, the rim in Sample DDM3-3-418 is Cu-rich (see below), and this may result from the incorporation of Cu into pyrite from a Cu-bearing fluid of Stage V (Fig. 5E). Based on the discussion above, we consider that the rims of these pyrite samples probably belong to Stage V.

4.1.2. Stage V: sulfide mineralization

The $\delta^{34}S$ values of both pyrite (+4.7‰ to +7.8‰; Figs. 4D, 5D, E) and chalcopyrite (+6.0‰ to +6.5‰; Figs. 4E and 5E) are highly homogeneous. Within the same sulfide grain, the pyrite $\delta^{34}S$ are slightly higher than those of chalcopyrite, again consistent with

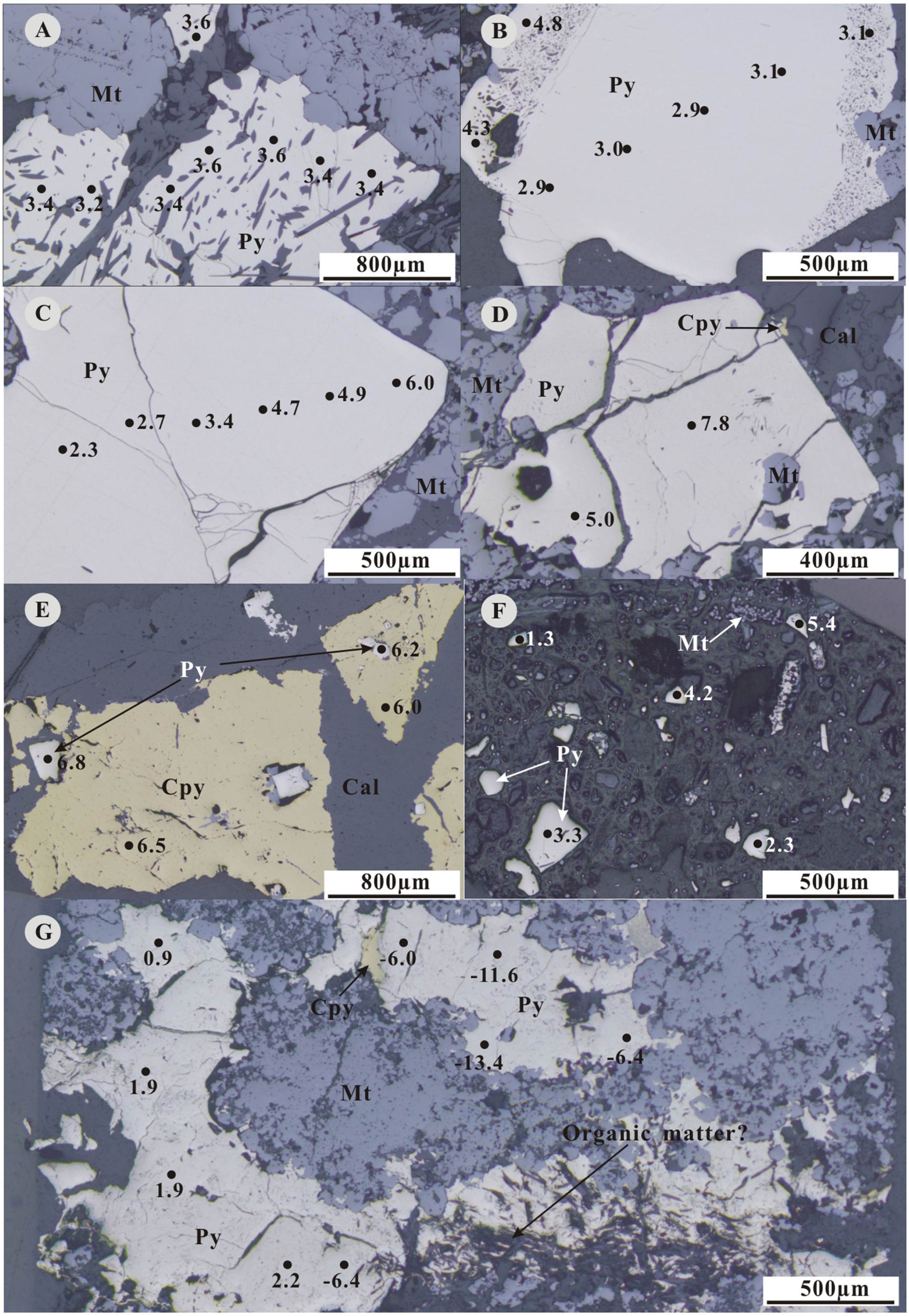

Fig. 5. Spots of in-situ sulfur isotopes of the Marcona sulfides. (A): Sample DDM3-3-34 (Stage IV). (B): Sample DDM3-3-418 (Stage IV). (C): Sample DDM-22-268. (D): Sample MA2-14 (Stage V). (E): Sample DDM4-7-338 (Stage V). (F): Sample DDM4-6-124 (Stage VII). (G): Sample DDM4-6-160 (Stage VII) Py: pyrite, Cpy: chalcopyrite, Cal: calcite, Mt: magnetite.

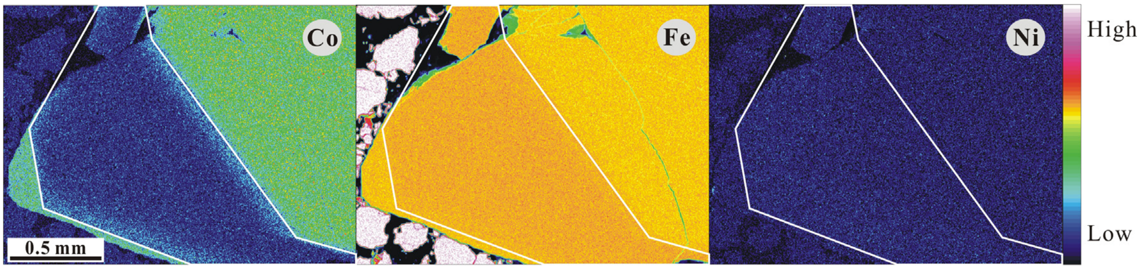

Fig. 6. WDS mapping of Co, Fe and Ni (DDM-22-268).

what is typically found for the chalcopyrite and pyrite that formed together (Bachinski, 1969; Kajiwara and Krouse, 1971).

4.1.3. Stage VII: late veins

Stage VII pyrite is featured by its wide δ^{34}S range. For the Sample DDM4-6-124, the δ^{34}S variation is up to 4.1‰ along a distance of <0.6 mm, with the lowest δ^{34}S at +1.3‰ and the highest at +5.4 ‰ (Fig. 5F). For Sample DDM4-6-160, the δ^{34}S variation reaches 15.7‰ along a distance of <2 mm, with the lowest δ^{34}S at −13.4‰ and the highest at +2.3‰ (Figs. 4F, 5G).

4.2. LA-ICP-MS sulfide geochemistry

4.2.1. Stage IV

In Stage IV pyrite, Co concentrations (449–19,618 ppm; median: 977 ppm) are highly variable, and broadly higher than Ni (19–974 ppm; median: 721 ppm) (Table 1). When individual pyrite grain is considered, Co concentration in Sample DDM-22-268 decreases from the core to the inner rim, and increases from the inner to the outer rim. Nickel and Fe concentrations vary in an opposite trend, although not as apparent as that of Co (Fig. 6, Table 1). Consequently, high Co/Ni ratios appear in the core (>100) and outer rim (>10), whereas low Co/Ni ratios (<1) appear in inner rim of this grain (Fig. 7). For Sample DDM3-3-418, the Co-Ni rich core is surrounded by a rim rich in Mn, Cu, Ag, Sb, Te, Pb and Bi, which also shows apparent Co-As enrichment in the outmost part of the rim (Fig. 8). Also, both DDM-22-268 and DDM3-3-418 show certain Se enrichment in the crystal rim (Table 1), and such variations of Se concentration and Se/S ratios are accompanied by a δ^{34}S increase (Fig. 9A).

Silver and Zn are enriched in Stage IV chalcopyrite (>100 ppm) (Fig. 10B), which contains no visible Ag-Zn-rich inclusion based on the generally smooth spectrum (Fig. 11A). Concentrations of Co, Ni, Se, Sn and Sb in Stage IV chalcopyrite are lower than that of Stage V (Fig. 10B, Table 1). Lead concentration has a relatively wide range, with one sample <10 ppm (δ^{34}S = +0.2‰) and another as high as 81 ppm (δ^{34}S value = +3.0‰). The most abundant trace elements in Stage IV pyrrhotite are Co and Ni (>100 ppm), and concentrations for As, Ag, Se, Pb, Mn and Bi are relatively low (<30 ppm) (Table 3).

4.2.2. Stage V

The Stage V pyrites are rich in Co (2993–12,403 ppm; median: 6841 ppm), Ni (113–585 ppm; median: 201 ppm), Cu

Table 1
Trace elements of pyrite at Marcona (ppm).

Stage	δ^{34}S	Sample	Mn	Co	Ni	Cu	Zn	As	Se	Ag	Sn	Sb	Te	Tl	Pb	Bi
Stage IV	2.3	DDM-22-268-Py-10	<0.6515	18,339	20	0.2150	0.7109	316.1241	5	<0.0346	<0.0661	<0.0484	<0.1763	<0.0110	<0.0479	<0.0104
	2.4	DDM-22-268-Py-9	2.9303	19,618	19	6.3970	0.7940	326.2799	9	0.2477	<0.0577	0.2496	0.1694	<0.0109	1.5017	0.0631
	2.7	DDM-22-268-Py-8	<0.5705	18,389	23	<0.2739	0.5568	288.3824	7	<0.0416	<0.0348	<0.0545	<0.3965	<0.0079	<0.0410	0.0021
	3.4	DDM-22-268-Py-7	<0.5022	4846	178	<0.2059	<0.5175	86.7711	5	0.0258	<0.0601	<0.0672	0.0740	<0.0276	<0.0456	<0.0128
	4.5	DDM-22-268-Py-6	<0.6198	1173	334	<0.3487	0.9316	48.2250	8	<0.0448	<0.0657	<0.0832	<0.4617	<0.0084	<0.0435	<0.0081
	4.7	DDM-22-268-Py-5	<0.5595	957	441	0.2998	0.5820	67.6329	7	<0.0215	0.0653	<0.0422	<0.1845	<0.0162	<0.0367	<0.0172
	4.8	DDM-22-268-Py-4	0.5147	998	662	<0.2440	0.9304	88.6597	7	<0.0859	<0.0646	<0.0811	<0.2004	<0.0194	<0.0459	<0.0084
	5.9	DDM-22-268-Py-3	<0.6841	1411	883	<0.3093	<0.6606	56.9714	7	<0.0236	<0.0498	<0.0480	0.2770	<0.0175	<0.0606	0.0023
	3.2	DDM3-3-418-Py5	<0.6148	449	812	<0.2159	<0.5790	22.1687	11	<0.0512	<0.0522	<0.0898	<0.2805	<0.0091	0.0451	0.0035
	3	DDM3-3-418-Py6	<0.5687	485	781	<0.2345	0.5902	26.5671	14	0.0184	0.0539	<0.0746	<0.2739	<0.0089	<0.0440	<0.0164
	3	DDM3-3-418-Py7	<0.6525	568	904	<0.2222	0.6622	27.0949	13	<0.0494	<0.0682	<0.0508	0.2951	<0.0137	<0.0547	0.0025
	3.1	DDM3-3-418-Py8	0.5739	624	902	<0.2062	0.7655	27.0486	13	0.0094	0.0611	<0.0297	<0.6341	<0.0268	<0.0644	<0.0117
	2.9	DDM3-3-418-Py9	0.5487	660	975	<0.2074	<0.8315	31.5023	14	<0.0214	<0.0662	<0.0862	<0.1870	<0.0221	<0.0476	<0.0132
	3	DDM3-3-418-Py10	0.6435	581	961	0.1675	<0.6037	28.3820	11	<0.0287	<0.0647	<0.0489	<0.3812	0.0057	<0.0455	0.0041
Stage V	6.1	DDM-22-268-Py-2	<0.4653	6212	585	<0.2897	1.1097	165.4030	8	0.0032	<0.0856	<0.0602	0.3249	<0.0085	<0.0512	<0.0083
	6.2	DDM-22-268-Py-1	<0.6344	12,403	167	<0.2146	<0.6763	230.1945	11	0.0129	0.0583	<0.0301	<0.1999	<0.0086	<0.0555	<0.0248
	4.8	DDM3-3-418-Py1	11.3404	7471	113	2918.0393	6.1400	217.7443	20	5.8093	<0.0889	4.7316	5.0962	<0.0240	15.1883	8.4593
	4.3	DDM3-3-418-Py2	<0.9945	2993	236	2197.4834	<0.8926	107.8652	13	3.4477	0.0839	1.4330	<0.6866	<0.0168	5.0782	0.9675
Stage VII	-9	DDM4-6-160-1-Py1	7.1823	333	1860	<0.2100	0.5347	0.8709	13	0.3192	<0.0633	1.0471	1.1318	0.1249	2.0917	0.0196
	-3.3	DDM4-6-160-1-Py2	17.1455	305	1690	<0.2645	0.9154	<0.2751	16	0.5057	0.0618	0.8074	0.7769	0.0898	4.4557	0.0156
	-3.4	DDM4-6-160-1-Py3	11.1291	693	4343	0.7729	0.8523	0.2736	30	1.6415	0.0643	3.1314	1.9604	0.2503	29.0832	0.0217
	-3.5	DDM4-6-160-1-Py4	15.5106	358	1902	<0.2120	0.7269	<0.2074	16	0.2087	0.0548	2.0117	1.8331	0.1635	1.4054	0.0115
	-0.8	DDM4-6-160-1-Py5	3.3946	312	1800	<0.2261	0.9455	0.4775	20	0.2999	0.0626	2.0119	0.5388	0.0548	2.4718	0.0108
Stage VII	2	DDM4-6-160-1-Py6	16.0996	257	1475	0.3799	0.5981	<0.2399	18	0.5669	0.0578	5.2225	1.0753	0.4665	3.4399	0.0164
	1.9	DDM4-6-160-1-Py7	11.5890	356	1833	7.2229	0.5760	0.3490	18	0.5474	0.0536	6.7960	1.1376	0.2881	9.7192	<0.0116
	1.9	DDM4-6-160-1-Py8	3.8082	634	4028	0.2449	0.8361	0.8812	30	0.8360	<0.0436	11.1922	1.5941	1.1341	32.7851	0.0117
	1	DDM4-6-160-1-Py9	11.4003	681	2410	24.8576	0.7365	7.6685	19	2.6457	<0.0546	10.4276	2.0472	0.3737	31.0150	0.1094
	-6	DDM4-6-160-1-Py10	18.2747	340	1927	<0.2147	3.3219	0.2918	16	0.4268	<0.0570	3.9849	1.8039	0.6372	5.9167	0.0237

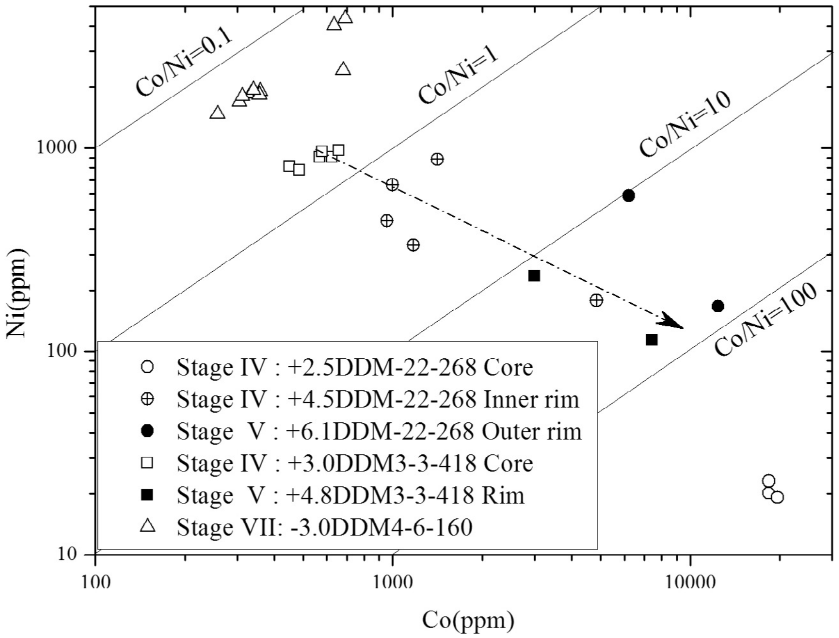

Fig. 7. Co/Ni ratios of the Marcona pyrite.

(2197–2918 ppm; median: 2558 ppm) and As (108–230 ppm; median: 192 ppm) (Fig. 10A), but poor in Se (8–20 ppm), Ag (0–6 ppm), Sb (0–5 ppm), Pb (0–15 ppm) and Bi (0–8 ppm) (Table 1). Compared with Stage IV chalcopyrite, Stage V chalcopyrite is also Zn-Ag-rich (in ppm: Zn, 495–784, median 545; Ag, 331–389, median 378) (Fig. 10B, Table 2), and Co-Ni-Se-Cd-Sn-poor (in ppm: Co < 1; Ni < 15; Se < 30; Cd < 6; Sn < 10). Concentrations of Sn, Sb, Te, Au, Tl, Pb and Bi of chalcopyrite at this stage are slightly higher than those of Stage IV (Fig. 10B, Table 2).

4.2.3. Stage VII

Stage VII pyrite is rich in Co (257–693 ppm), Ni (1475–4343 ppm) and poor in As (<8 ppm) (Fig. 10A, Table 1). Compared with Stage IV pyrite (Fig. 10A, Table 1), the concentration of Mn (3–18 ppm), Se (13–30 ppm), Sb (1–10 ppm), Tl (1 ppm) and Pb (1–35 ppm) of Stage VII pyrite are relatively high.

5. Discussion

5.1. Source and evolution of ore-forming fluids

Given the Stage IV temperature range (430–600 °C, Chen et al., 2011) and low fO_2 (the pyrite-pyrrhotite buffer in Ohmoto, (1979)), the $\delta^{34}S$ difference between the sulfides and ore-forming fluids would be negligible (Ohmoto, 1979). Thus, the ore-forming fluids of Stage IV may have had $\delta^{34}S$ of +0.5‰ to +3.5‰, suggesting a magmatic origin (Ohmoto, 1979; Seal, 2006).

Stage IV pyrite contains a very homogeneous core in terms of both $\delta^{34}S$ value and trace elements (Figs. 5B, 8), suggesting stable physicochemical condition of the ore-forming fluids when the core was formed. The $\delta^{34}S$ values show a sharp rise from +2.9‰ (core) to +4.8‰ (rim) (Fig. 5B), and the trace element concentrations also change dramatically (Fig. 8): the core is Co-Ni-rich and depleted of other elements, whereas the rim is relatively Co-Ni-poor and contains higher Mn, Cu, Ag, Sb, Te, Pb and Bi. We propose that this abrupt $\delta^{34}S$ and trace element change may have been caused by external fluid incursion. For Sample DDM-22-268 (Stage IV pyrite), $\delta^{34}S$ increase from +2.3‰ (core) to +6.0‰ (rim) (Fig. 5C). The pyrite core is Co-rich and Ni-Fe-poor, the inner rim is Ni-Fe-rich and Co-poor, whereas the outer rim is again Co-rich and Ni-Fe-poor. This shows a consecutive substitution of Fe by Co → Ni → Co in the pyrite crystal lattice. As suggested by Deditius et al. (2009), this consecutive Fe substitution was unlikely to have happened in a fluid system with stable temperature and fluid compositions. Fitzpatrick (2008) suggested that at above 350 °C, ^{34}S would be preferentially partitioned into pyrite relative to Se, which would increase the $\Sigma Se/\Sigma S$ ratio of the fluids. If the system is closed, the early-formed pyrite would have high $\delta^{34}S$ and low Se/S, and vice versa for the later-formed pyrite, thus forming a negative $\delta^{34}S$ vs. Se/S correlation. Both Samples DDM3-3-418 and DDM-22-268 show positive $\delta^{34}S$ vs. Se/S correlation (Fig. 9A), indicating that the system was open. The mass $\sum Se/\sum S$ ratio of magmatic fluids ($1.2–5 \times 10^{-4}$) is substantially different from that of seawater ($5–25 \times 10^{-8}$) (Huston et al., 1995), hence the sulfide Se/S ratio can serve as a proxy for the relative contributions of fluid sources. Magmatic fluids and modern seawater commonly have $\delta^{34}S$ at around 0‰ and +21‰ (Seal, 2006), respectively. All our Marcona sulfide data lie between these two sources, and fall on a smooth trend (Fig. 9A), which supports the incursion and mixing of external fluids (possibly seawater) into the ore-fluid system. Seawater incursion would increase the oxygen fugacity (fO_2) of ore-forming fluids and thus the Se/S ratios, since Se prefers to enter high fO_2 system (Fitzpatrick, 2008). In short, we propose that the ore-forming fluids formed in an open system, and that the $\delta^{34}S$ and trace element zonation in some Stage IV pyrites may have resulted from the late-stage incursion and mixing of non-magmatic external fluids (e.g., seawater). Although the sulfur isotopic features from Marcona sulfides can also indicate source of evaporates, we consider that ore-forming fluids may directly come from external fluids (i.e., basinal brines or residue seawater), which is supported by: (1) there is no Mesozoic evaporate documented in this region; (2) the Marcona deposit formed during the initial opening of the Cañete basin (Chen et al., 2010b) and evaporate is unlikely formed during that stage.

Pyrite formed in sedimentary environments usually contains low Co and Ni, with Co/Ni < 1 (Loftus-Hills and Solomon, 1967), whereas volcanogenic pyrite usually contains high Co and Ni, with Co/Ni > 1 (Loftus-Hills and Solomon, 1967; Price, 1972; Bralia et al.,

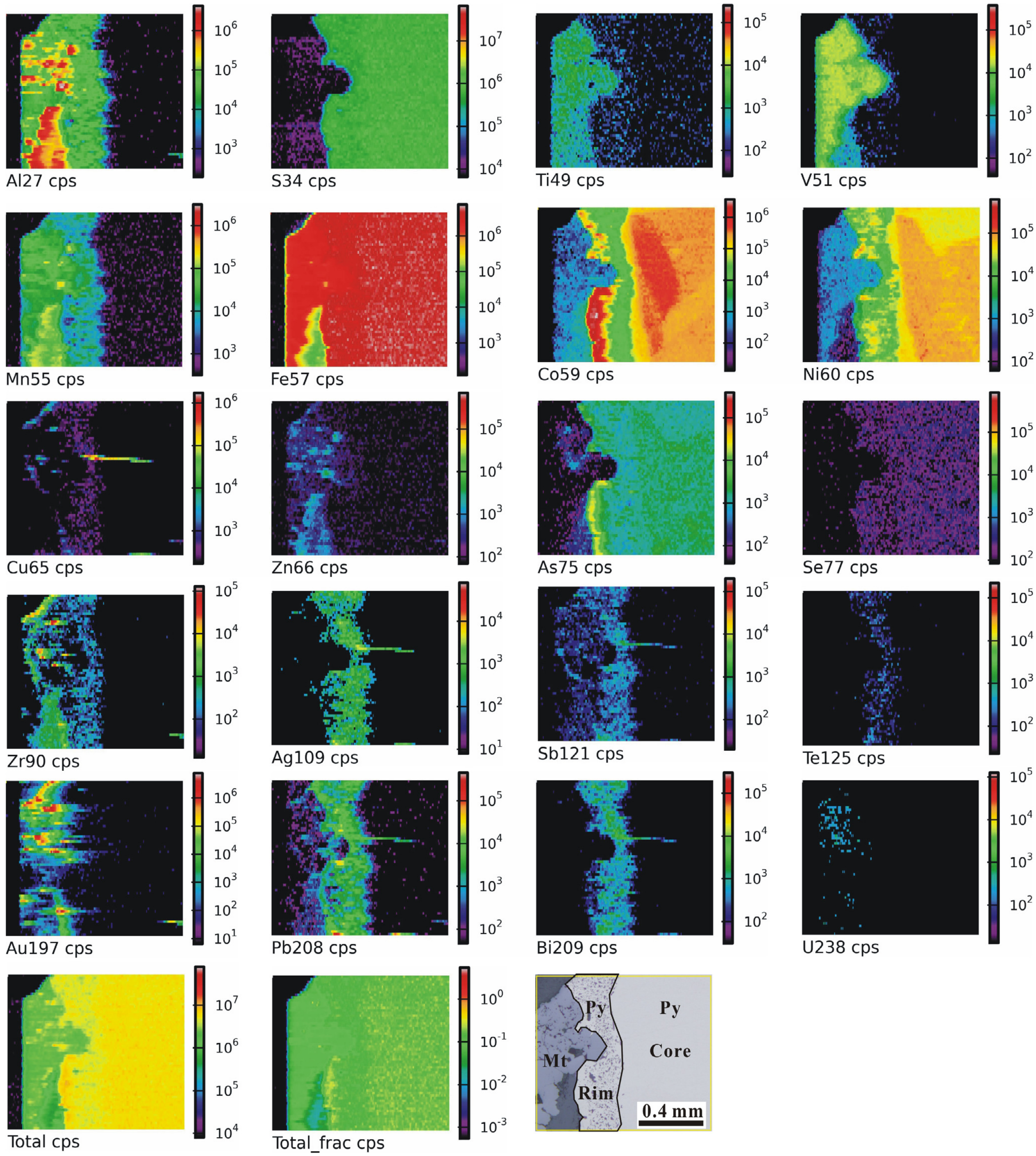

Fig. 8. LA-ICP-MS mapping of sample DDM3-3-418 pyrite.

1979). Hydrothermal pyrite usually contains highly variable Co and Ni, and hence Co/Ni is also variable but typically > 1 (Bralia et al., 1979; Cook, 1996; Zhao et al., 2011; Li et al., 2014).

As for Stage IV sample DDM-22-268, the Co-rich and Ni-poor core shows highly elevated Co/Ni values (>100) (Fig. 7). The elevated Co/Ni and low $\delta^{34}S$ (<+3.0‰) indicate that the pyrite core was grown in a magmatic-hydrothermal fluid under high temperature (430–600 °C; Chen et al., 2011) and fS_2 conditions (Fig. 12). The inner rim has higher $\delta^{34}S$ than the core, implying gradual incursion of external fluids (probably seawater). The initial seawater incursion may have decreased the temperature but not apparently changed the fS_2 of the fluid system (Fig. 12), resulting in more Ni substitution (for Fe in pyrite) and lower Co/Ni ratios (< 1) (Fig. 7). With continuing seawater incursion, both temperature (160–360 °C at Stage V; Chen et al., 2011) and fS_2 decreased (Fig. 12), resulting in the Co substitution (for Fe in pyrite) and increase Co/Ni ratios (>10) (Fig. 7). For another Stage IV sample DDM3-3-418, the pyrite core is also $\delta^{34}S$ (<+3.0‰) and trace

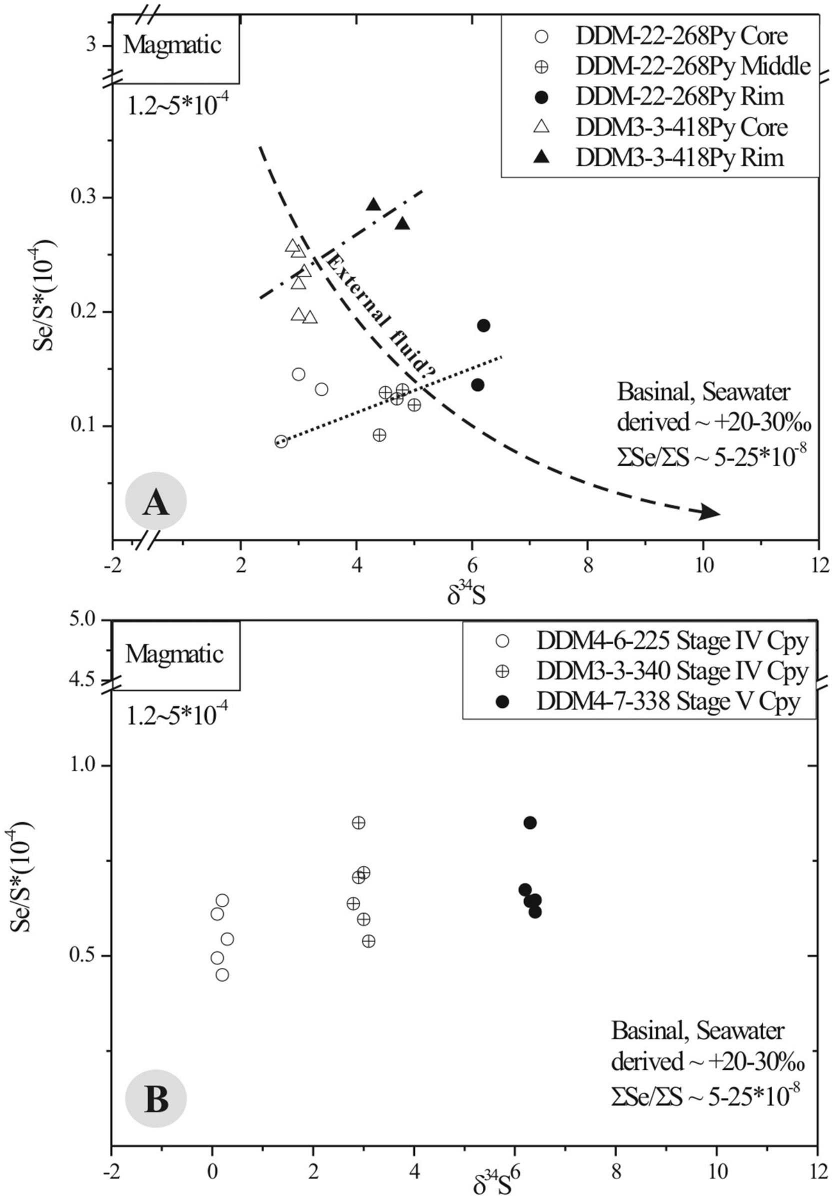

Fig. 9. Se/S ratios of (A) pyrite and (B) chalcopyrite.

element homogeneous, indicating a stable ore-forming fluid environment. The sharp δ^{34}S increase (+4.8‰) and enrichments in Mn, Cu, Ag, Sb, Te, Pb and Bi in the thin pyrite rim resemble typical diagenetic pyrite (Large et al., 2009; Agangi et al., 2013), indicating significant external fluid contribution.

δ^{34}S values of Stage V pyrite and chalcopyrite are mostly above +5.0‰ (Fig. 4D, E). The paragenetic mineral assemblage (Py + Cpy ± Po) and temperature (160–360 °C, Chen et al., 2011) at this stage suggest that the δ^{34}S difference between the sulfides and ore-forming fluids would be negligible (Ohmoto, 1979). Consequently, the ore-forming fluids of Stage V may have resulted from significant contribution of non-magmatic fluids, which may have reacted with the andesitic host rocks. Furthermore, the Se/S ratios of Stage V chalcopyrite are higher than those of Stage IV (Fig. 9B). As mentioned before, the elevated Se/S may have led by the rise of fO_2 derived from seawater. The elevated δ^{34}S of both pyrite and chalcopyrite (Fig. 4D, E) and the enrichments of Sb, Te, Pb and Bi (Fig. 10B) in chalcopyrite also support this interpretation.

At Stage VII, the pyrite δ^{34}S change > 15.0‰ along a distance of <2 mm, and mostly characterized by negative δ^{34}S (as low as −13.4‰). There are many submicrometer-size voids (Fig. 13A) disseminated in Stage VII pyrite, and we suggest that these voids may represent the site where the organic matter occurs. Additionally, Stage VII pyrite is rich in trace elements (e.g., Mn, Se, Sb, Te, Tl and Pb), and has heterogeneous internal structure (Fig. 13A), both indicating possible fast precipitation. The ragged LA-ICP-MS signal (Fig. 11B), indicative of heterogeneous trace element distribution, maybe a result of the present of micron size magnetite inclusions (Fig. 13B) and organic matter. In addition, all the Co/Ni values of Stage VII pyrite are <1 (average at 0.2) (Fig. 7), resembling the pyrite of sedimentary environment. Based on the above discussions, we propose that Stage VII pyrite was rapidly deposited from disequilibrated fluid with involvement of organic material. Rapid precipitation processes may have incorporated trace elements into the pyrite structure and caused great δ^{34}S variation.

We also noticed that both Stage IV and V chalcopyrite are Zn-Ag-rich (Fig. 10B, Table 2). At Stage V, Zn (average at 604 ppm)

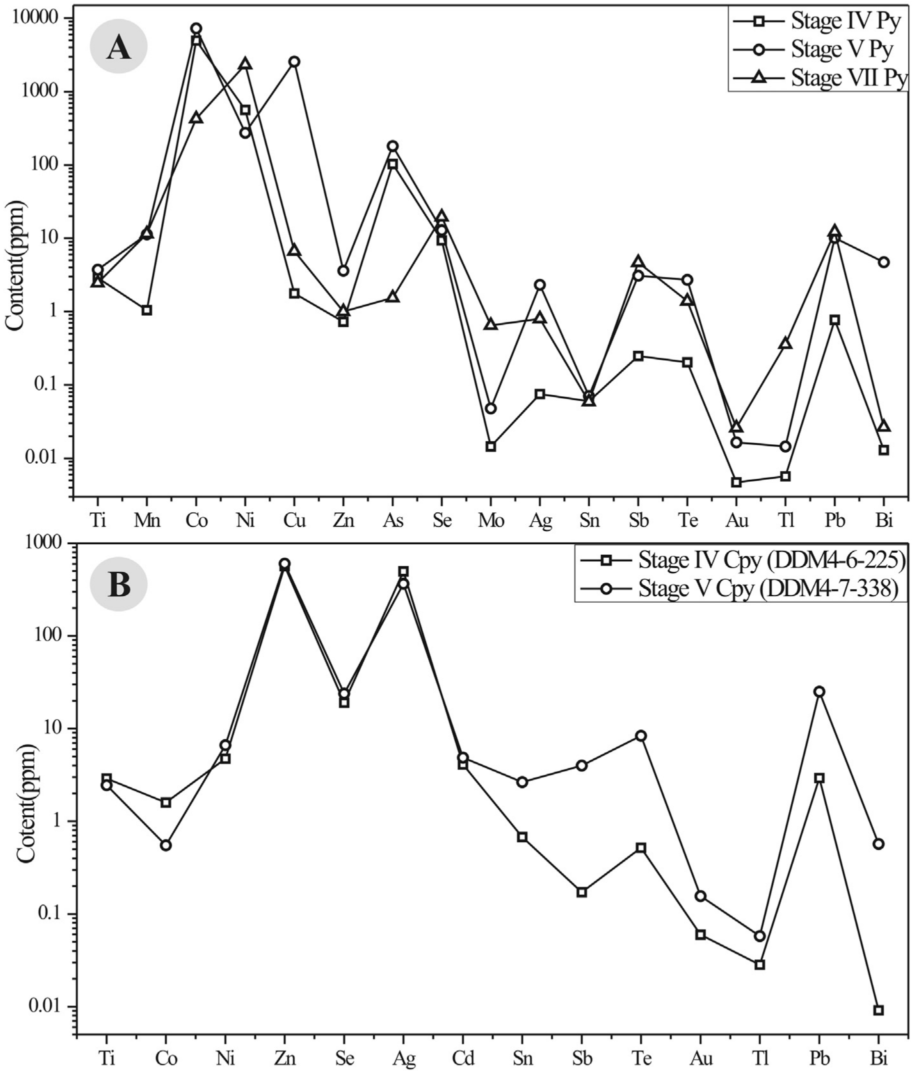

Fig. 10. Trace element concentrations of the different-stage sulfides: (A) Stages IV, V and VII pyrite. (B) Stages IV and V chalcopyrite.

and Ag (average at 366 ppm) concentrations are generally higher than those of Stage IV (Zn average at 385 ppm and Ag 276 ppm). It is most likely that Ag substituted Cu in the chalcopyrite lattice (Fig. 11A), possibly due to the identical charge and similar ionic radius of Ag^+ (1.15 Å) and Cu^+ (0.77 Å) (George et al., 2016). Zinc enrichment in chalcopyrite can be resulted by the substitution of Fe due to their similar ionic radius (Zn^{2+}: 0.60 Å; Fe^{2+}: 0.63 Å) (George et al., 2016). Higher Ag and Zn in Stage V chalcopyrite may indicate a possible Cu-Ag-Zn source from low-temperature external fluids, similar to some IOCG deposits in the central Andes, such as Mantoverde and Mina Justa (Chen et al., 2011; Chen, 2013), and this also supports our suggestion of incursion of external fluids at late Stage IV and Stage V.

5.2. Metallogenic process

The Pacific Plate subduction beneath the western South American Plate has led to regional extension, which attenuated the arc crust and generated deep-sourced andesitic magmatism (Sillitoe, 2003). During this process, the Cañete basin and the upper-Río Grande Formation were formed (Chen et al., 2010b). Extensive andesitic magmatism may have brought large volume of magmatic fluids, from which the Marcona massive magnetite and sulfide (Stage IV) orebodies may have formed (ca. 161–159 Ma; Chen et al., 2010b). At early Stage IV, the major ore-forming fluids were magmatic with high temperature, and the pyrite formed contains Co/Ni ratios > 100 (Fig. 7) and $\delta^{34}S$ values mostly <+3.5‰ (Fig. 4A). The normal faults formed under the extensional tectonic regime may have served as conduits for the external non-magmatic fluids (e.g., seawater) incursion. With the incursion of external fluid, the pyrite formed in late Stage IV has elevated $\delta^{34}S$ values and rich in Mn, Cu, Ag, Sb, Te, Pb and Bi. With cooling of magma, the temperature of fluid system decrease, and this allow massive incursion of external fluid, probably seawater, which may have reacted with the andesitic wall rocks and caused the pyrite and chalcopyrite precipitation. During Stage VII, some organic materials may have been incorporated into the hydrothermal system. With the help of residual magmatic heat, seawater was reduced and caused the precipitation of pyrite with very low and variable $\delta^{34}S$ (−13.4‰ to +2.3‰).

5.3. Implication for the genesis of Marcona sulfide mineralization and IOCG deposits

Even though the Marcona deposit is located in the iron oxide copper-gold province of southern Perú, and extensive magnetite

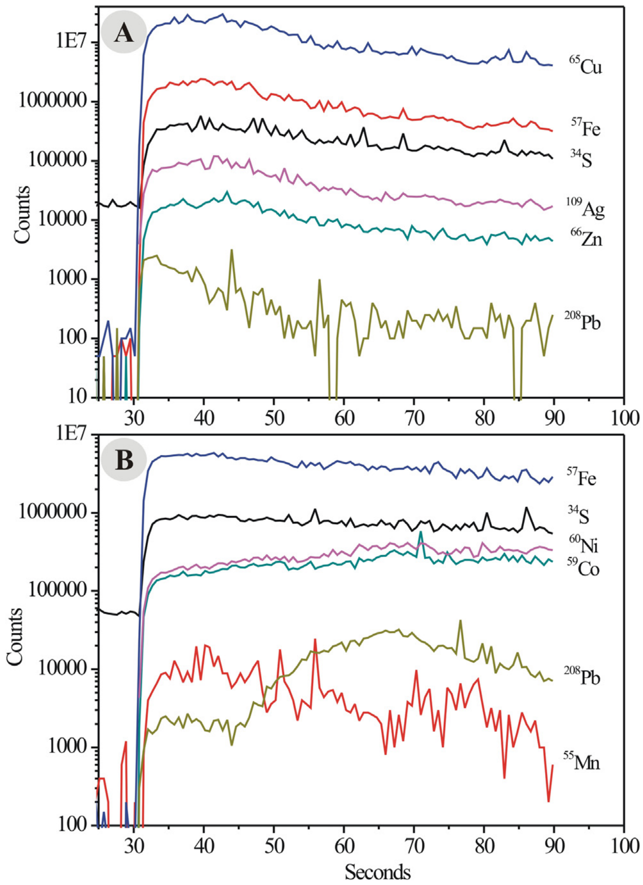

Fig. 11. LA-ICP-MS signal of (A) Stage IV chalcopyrite (sample DDM4-6-225) and (B) Stage VII pyrite (sample DDM4-6-160).

mineralization was observed (Chen et al., 2010b), economic Cu (-Au) mineralization and hydrothermal breccias, typical of IOCG deposits, are absent in the Marcona deposit. However, it shows some similarities with nearby Mina Justa deposit. First, both deposits exhibit extensive Na alteration (Stage II at Marcona and Stage III at Mina Justa), followed by massive iron oxide mineralization (Stage III to IV at Marcona and Stage V at Mina Justa) (Chen et al., 2010b). Second, the ore-forming fluids sources in both deposits were initially magmatic, with external fluids evolved into ore-forming fluid system at late stage (Chen et al., 2011). Third, higher Ag and Zn in Stage V chalcopyrite (Fig. 10B) at Marcona may indicate a possible Cu-Ag-Zn source from low-temperature external fluids, similar to what was documented at Mina Justa (Chen et al., 2011).

One of the most important issues on IOCG genesis is the incursion of external fluid and its effect on Cu (-Au) mineralization (Chen, 2013). Previous studies have documented that most major Cu-rich IOCG centres derived external sulfur from either surficial basinal brines and seawater (Benavidies et al., 2007; Chen et al., 2011; Haynes et al., 1995; McPhie et al., 2011; Zhao et al., 2017) or formation water and metamorphic fluids (Mitchell and Krouse, 1975), or from lithologies (Chen and Zhou, 2012). In this study, the δ^{34}S values of ore-forming fluid in Cu-barren Stage IV are mainly <+4.0‰, indicating a major magmatic origin. At late of this stage the fluid system underwent apparent external fluid incursion and the δ^{34}S values of pyrite increase rapidly from +2.3‰ to +6.0‰. In the subsequent polymetallic sulfide mineralization stage (Stage V), in which chalcopyrite and pyrite were deposited, the δ^{34}S values of the ore-forming fluid are mainly around +6‰, supportive of an exotic source of sulfur. We think that the external fluid incursion may be directly related to and played an important role on the Stage V sulfide mineralization. Similar with Marcona deposit, the nearby Mina Justa IOCG deposit also witnessed the incursion of external fluids, mainly in the Cu mineralization stage (Stage J-VI, Chen et al., 2011). All of this evidence support that addition of external sulfur into an originally sulfur-poor system may have triggered massive Cu (-Au) mineralization after iron oxide deposition in many IOCG systems.

6. Conclusions

(1) As shown by the magmatic-like δ^{34}S signature of pyrite, the Marcona ore-forming fluids of Stage IV may have been primarily magmatic. The elevated δ^{34}S, abrupt Co/Ni drop and the positive δ^{34}S vs. Se/S correlation in the pyrite inner rim suggest the probable incursion of external non-magmatic fluids (probably seawater). The higher δ^{34}S of Stage V sulfides and enrichment of Mn, Cu, Ag, Sb, Te, Pb and Bi in Stage V pyrite and chalcopyrite resemble typical diagenetic pyrite and suggest that the ore-forming fluid at this stage is mainly sedimentary-derived. The negative δ^{34}S, wide δ^{34}S range, and enrichment of Mn, Se, Sb, Te, Tl and Pb concentrations of Stage VII pyrite may have been derived from the reduction of organic matter.

Table 2
Trace elements of chalcopyrite at Marcona (ppm).

Stage	δ^{34}S	Sample	Ti	Mn	Co	Ni	Zn	Se	Ag	Cd	Sn	Sb	Te	Au	Tl	Pb	Bi
Stage IV	0.2	T301DDM4-6-225-Ccp1	3.1233	<0.9494	1.2878	4.3584	481	21	487	4.2081	0.7801	<0.1460	<0.3879	0.0762	<0.0586	2.0866	0.0046
		T301DDM4-6-225-Ccp2	2.4451	<1.0910	1.2635	7.5658	527	17	488	3.5758	0.6521	0.1721	0.5108	0.0675	0.0478	6.3021	<0.0321
		T301DDM4-6-225-Ccp3	3.1264	<0.8333	1.8434	3.4391	627	22	500	4.4621	0.7211	<0.1304	<0.7793	<0.0469	<0.0368	2.0303	0.0137
		T301DDM4-6-225-Ccp4	<2.9111	1.0300	1.8959	4.2146	628	16	495	4.1698	0.6830	<0.1629	0.5236	0.0507	0.0090	1.9569	<0.0168
		T301DDM4-6-225-Ccp5	<2.0104	<0.9817	1.6709	4.1705	576	19	516	4.0994	0.5560	<0.0922	<0.3800	0.0445	<0.0392	1.9218	<0.0163
	3	DDM3-3-340-Ccp1	<3.2000	2.7538	0.4159	0.0557	238	22	96	2.6565	5.1369	0.8149	9.8298	0.0561	0.0363	57.1984	1.0218
		DDM3-3-340-Ccp2	<4.8467	2.7508	0.3016	<0.1950	240	21	94	2.1679	5.9734	0.5987	9.1253	0.0740	0.0307	81.4926	0.9557
		DDM3-3-340-Ccp3	2.4959	6.3968	0.2715	<0.2597	229	25	92	2.6060	5.8856	0.3311	7.1448	<0.0796	<0.0317	76.0644	0.4129
		DDM3-3-340-Ccp4	<2.3982	6.7437	0.2451	<0.1451	268	19	93	2.1105	7.1070	0.2793	11.5672	<0.0403	<0.0425	56.2187	0.5791
		DDM3-3-340-Ccp5	5.4600	2.9635	0.3968	0.2611	213	25	85	1.7333	0.8217	1.3583	4.2377	<0.0570	<0.0357	10.7935	0.6264
		DDM3-3-340-Ccp6	3.0263	1.0160	0.3462	<0.1861	211	30	86	1.8580	2.9584	1.1779	4.5969	<0.0373	0.0335	21.4380	0.8307
Stage V	6.3	DDM4-7-338-Ccp1	2.9364	1.6937	0.4879	1.2745	545	21	390	4.6456	8.5460	1.5372	10.7203	0.0183	0.0195	16.5142	0.1749
		DDM4-7-338-Ccp2	<1.3813	1.5773	0.4729	14.8956	785	22	378	5.6791	1.4565	2.7633	8.3527	<0.0727	0.0136	11.6999	0.3538
		DDM4-7-338-Ccp3	<4.2361	2.0665	0.6548	2.8741	543	30	378	5.2138	1.0266	6.2018	7.9313	0.0274	<0.0867	26.3410	1.0008
		DDM4-7-338-Ccp4	1.9712	1.1051	0.5986	8.4577	495	23	355	3.5588	0.5350	4.5754	9.2194	0.4225	0.1512	46.7290	0.4731
		DDM4-7-338-Ccp5	<3.2754	<1.1106	0.5415	5.6730	650	22	331	5.2604	1.6184	4.8759	5.5375	<0.0727	0.0463	17.9812	0.8379

Table 3
Trace elements of pyrrhotiteat Marcona (ppm).

Stage	$\delta^{34}S$	Sample	Mn	Fe	Co	Ni	Se	Ag	Te	Au	Tl	Pb	Bi	Th
Stage IV	0.8	T301DDM4-6-225-Po1	<1.2418	635,300	123	804	<13.0266	1.092019072	1.651222	<0.0579	<0.0000	2.847346	<0.0000	<0.0000
		T301DDM4-6-225-Po2	1.174993	635,300	138	901	20.51864	1.235560689	2.656024	0.015761	<0.0469	4.475914	0.031928	<0.0000
		T301DDM4-6-225-Po3	1.748349	635,300	134	797	14.8315	3.029049245	1.124456	0.014065	0.005186	2.733549	0.010264	<0.0490
		T301DDM4-6-225-Po4	2.046462	635,300	126	246	14.98093	3.400304962	0.725247	<0.0485	<0.0499	18.75399	<0.0000	<0.0329
		T301DDM4-6-225-Po5	1.409683	635,300	159	344	29.56742	3.661046487	<1.1389	<0.0549	<0.0404	25.88438	<0.0196	<0.0000
	1	T301MA5-2-Po1	7.812345	635,300	897	1914	26.42792	0.162937842	2.002191	<0.0618	<0.0315	1.146855	0.180802	<0.0390
		T301MA5-2-Po2	7.05375	635,300	837	1785	23.42554	<0.0811	1.805057	<0.0585	<0.0213	0.403828	0.069148	<0.0366
		T301MA5-2-Po3	10.6923	635,300	893	1890	31.34381	0.066327873	1.93295	0.016829	<0.0312	0.191011	0.049394	<0.0839
		T301MA5-2-Po4	8.159379	635,300	828	1797	16.59314	0.048331445	2.935612	<0.1342	<0.0220	0.62252	0.088563	<0.0371
		T301MA5-2-Po5	4.601203	635,300	909	2021	19.52084	0.170335517	2.279985	<0.0000	<0.0399	2.317746	0.387947	<0.0393
	2.9	T301DMA27-526.9-Po1	2.635101	635,300	1034	1347	26.31348	1.201642567	<1.1453	0.024883	<0.0444	16.31084	0.899497	0.005534
	3	T301DMA27-526.9-Po2	12.07999	635,300	823	1725	25.17017	0.942623281	<1.1034	0.01613	<0.0459	17.15626	0.707407	0.005334
	4.5	T301DMA27-526.9-Po3	2.910149	635,300	1016	1154	11.16494	0.397818652	1.305819	0.015462	<0.0457	3.470135	0.175095	0.005067
	4.7	T301DMA27-526.9-Po4	3.905887	635,300	965	1187	12.84364	0.103876105	2.245435	0.053857	0.014097	1.928757	0.108876	0.004996
	4.7	T301DMA27-526.9-Po5	3.198925	635,300	1007	1122	<9.4829	0.073316487	1.242799	0.023679	0.03769	1.656137	0.094171	<0.0370
	4.4	T301DMA27-526.9-Po6	4.722692	635,300	1050	1084	10.87015	<0.1253	1.177448	<0.0000	0.003101	2.231964	0.1259	0.016211

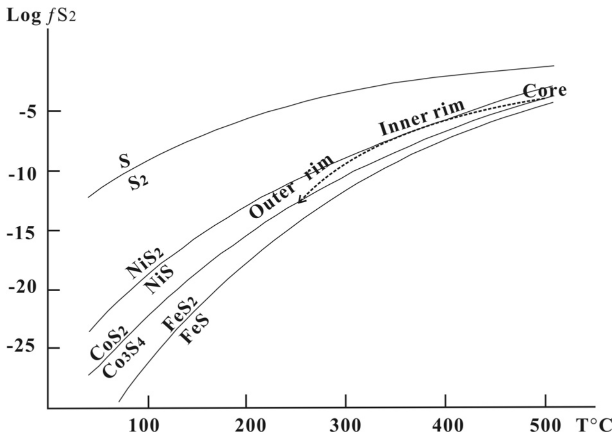

Fig. 12. fS_2 vs. T°C diagram (modified after Eremin, 1983 and Maslennikov et al., 2009) for the DDM-22-268 pyrite core, inner and outer rim.

(2) Sulfide mineralization at Marcona deposit shares similarities with IOCG deposits, with involvement of external fluids during the sulfide stages, but hydrothermal breccias and Cu-mineralization, typical signatures of IOCG deposits, were only locally developed. Our findings support that the Marcona deposit share similarities on ore genesis with the nearby Mina Justa IOCG deposit.

Acknowledgements

We thank Professor Franco Pirajno and the anonymous reviewer for detailed reviews and constructive suggestions. This research was jointly supported by Guangzhou municipal government (201607020029), the Chinese National Basic Research 973-Program (2014CB440802), National Natural Science Foundation of China (41572059), CAS-SAFEA International Partnership Program for Creative Research Team (20140491534) and CAS 100 talent program (Y333081A07). We would like to thank Chao Wu for the LA-ICP-MS analysis and Chang-Ming Xing for the EMPA analysis. This is contribution No. IS-2359 from GIGCAS.

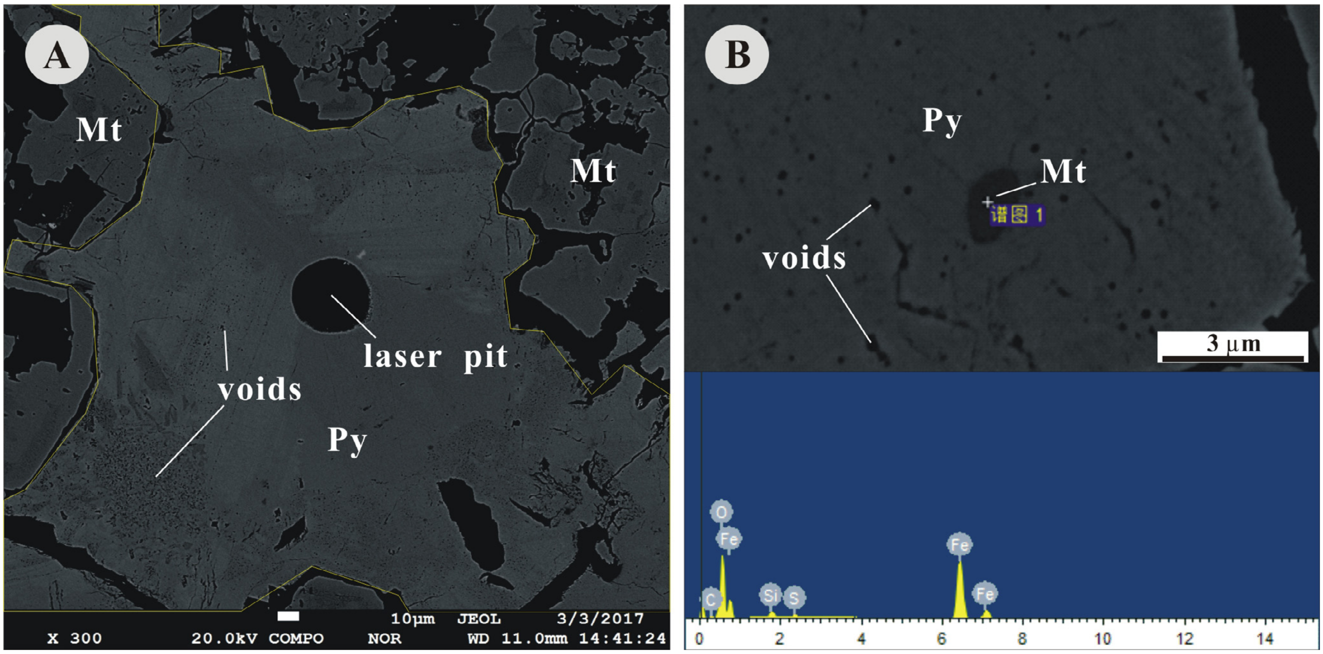

Fig. 13. BSE images show (A) complex internal structure and (B) magnetite inclusions and voids in pyrite of Stage VII.

References

Agangi, A., Hofmann, A., Wohlgemuth-Ueberwasser, C.C., 2013. Pyrite zoning as a record of mineralization in the Ventersdorp Contact Reef, Witwatersrand Basin, South Africa. Econ. Geol. 108, 1243–1272.

Atchley, F.W., 1956. Geology of the Marcona Iron Deposits, Peru. School of Mineral Sciences.

Atkin, B., Injoque, J., Harvey, P., 1985. Cu-Fe amphibole mineralization in the Arequipa segment. Magmatism at the plate edge: The Peruvian Andes. Blackie, Glasgow, UK, pp. 261–270.

Bachinski, D.J., 1969. Bond strength and sulfur isotopic fractionation in coexisting sulfides. Econ. Geol. 64, 56–65.

Baker, T., Perkins, C., Blake, K.L., Williams, P.J., 2001. Radiogenic and stable isotope constraints on the genesis of the Eloise Cu-Au deposit, Cloncurry district, northwest Queensland. Econ. Geol. Bull. Soc. Econ. Geol. 96, 723–742.

Benavides, J., Kyser, T.K., Clark, A.H., Oates, C.J., Zamora, R., Tarnovschi, R., Castillo, B., 2007. The Mantoverde iron oxide-copper-gold district, III region, Chile: the role of regionally derived, nonmagmatic fluids in chalcopyrite mineralization. Econ. Geol. 102, 415–440.

Bralia, A., Sabatini, G., Troja, F., 1979. A revaluation of the Co/Ni ratio in pyrite as geochemical tool in ore genesis problems. Miner. Deposita 14, 353–374.

Caldas Vidal, J., 1978. Geología de los cuadrángulos de San Juan, Acarí y Yauca: hojas, (31-m, 31-n, 32-n). Instituto de Geología y Minería, Lima, Peru.

Case, G., Chang, Z., Huizenga, J.M., Lilly, R., Blenkinsop, T., 2015a. The Evolution and Potential Sources of Mineralizing Fluids of the E1 Group of IOCG Deposits, Cloncurry District, Northwest Queensland, Australia: Implications from Fluid Inclusion and SHRIMP S Isotope Analyses.

Case, G., Stormont, E., Huizenga, J.M., Chang, Z., 2015b. Fluid Inclusion, Trace Element, and Isotopic Characteristics of Mineralization-associated Hydrothermal Barite in the Cloncurry IOCG District, Northwest Queensland.

Chen, H., Kyser, T.K., Clark, A.H., 2011. Contrasting fluids and reservoirs in the contiguous Marcona and Mina Justa iron oxide–Cu (–Ag–Au) deposits, south-central Perú. Miner. Deposita 46, 677–706.

Chen, H.Y., Clark, A.H., Kyser, T.K., 2010a. The Marcona magnetite deposit, Ica, South-Central Peru: a product of hydrous, iron oxide-rich melts? Econ. Geol. 105, 1441–1456.

Chen, H.Y., Clark, A.H., Kyser, T.K., Ullrich, T.D., Baxter, R., Chen, Y.M., Moody, T.C., 2010b. Evolution of the Giant Marcona-Mina Justa Iron Oxide-Copper-Gold District, South-Central Peru. Econ. Geol. 105, 155–185.

Chen, H.Y., 2013. External sulphur in IOCG mineralization: implications on definition and classification of the IOCG clan. Ore Geol. Rev. 51, 74–78.

Chen, L., Li, X.H., Li, J.W., Hofstra, A.H., Liu, Y., Koenig, A.E., 2015a. Extreme variation of sulfur isotopic compositions in pyrite from the Qiuling sediment-hosted gold deposit, West Qinling orogen, central China: an in situ SIMS study with implications for the source of sulfur. Miner. Deposita 50, 643–656. http://dx.doi.org/10.1007/s00126-015-0597-9.

Chen, W.T., Zhou, M.F., 2012. Paragenesis, stable isotopes, and molybdenite Re-Os isotope age of the Lala Iron-Copper Deposit, Southwest China. Econ. Geol. 107, 459–480.

Chen, W.T., Zhou, M.F., Gao, J.F., Hu, R., 2015b. Geochemistry of magnetite from Proterozoic Fe-Cu deposits in the Kangdian metallogenic province, SW China. Miner. Deposita 50, 795–809.

Chen, W.T., Zhou, M.F., Li, X., Gao, J.F., Hou, K., 2015c. In-situ LA-ICP-MS trace elemental analyses of magnetite: Cu-(Au, Fe) deposits in the Khetri copper belt in Rajasthan Province, NW India. Ore Geol. Rev. 65, 929–939.

Cobbing, E.J., 1999. The Coastal Batholith and other aspects of Andean magmatism in Peru. Geological Society London Special Publications 168, 111–122.

Cook, N.J., 1996. Mineralogy of the sulphide deposits at Sulitjelma, northern Norway. Ore Geol. Rev. 11, 303–338.

Danyushevsky, L., Robinson, P., Gilbert, S., Norman, M., Large, R., McGoldrick, P., Shelley, M., 2011. Routine quantitative multi-element analysis of sulphide minerals by laser ablation ICP-MS: standard development and consideration of matrix effects. Geochem.-Explor. Environ. A 11, 51–60.

Deditius, A.P., Utsunomiya, S., Ewing, R.C., Chryssoulis, S.L., Venter, D., Kesler, S.E., 2009. Decoupled geochemical behavior of As and Cu in hydrothermal systems. Geology 37, 707–710.

Eremin, N., 1983. Differentiation of Volcanogenic Sulfide Deposits. Moscow state University Press, Moscow.

Fitzpatrick, A.J., 2008.The Measurement of the Se/S Ratios in Sulphide Minerals and their Application to Ore Deposit Studies.

George, L.L., Cook, N.J., Ciobanu, C.L., 2016. Partitioning of trace elements in co-crystallized sphalerite-galena-chalcopyrite hydrothermal ores. Ore Geol. Rev. 77, 97–116. http://dx.doi.org/10.1016/j.oregeorev.2016.02.009.

Gilbert, S.E., Danyushevsky, L.V., Rodemann, T., Shimizu, N., Gurenko, A., Meffre, S., Thomas, H., Large, R.R., Death, D., 2014. Optimisation of laser parameters for the analysis of sulphur isotopes in sulphide minerals by laser ablation ICP-MS. J. Anal. At. Spectrom. 29, 1042–1051. http://dx.doi.org/10.1039/c4ja00011k.

Groves, D.I., Bierlein, F.P., Meinert, L.D., Hitzman, M.W., 2010. Iron oxide copper-gold (IOCG) deposits through earth history: implications for origin, lithospheric setting, and distinction from other epigenetic iron oxide deposits. Econ. Geol. 105, 641–654.

Hawkes, N., Clark, A., Moody, T., 2002. Marcona and Pampa de Pongo: giant Mesozoic Fe-(Cu, Au) deposits in the Peruvian coastal belt. Hydrothermal iron oxide copper-gold and related deposits: a global perspective, vol. 2. Porter Geoscience Consultancy Publishing, Adelaide, pp. 115–130.

Haynes, D.W., Cross, K.C., Bills, R.T., Reed, M.H., 1995. Olympic Dam ore genesis – a fluid-mixing model. Econ. Geol. Bull. Soc. Econ. Geol. 90, 281–307.

Hitzman, M.W., Oreskes, N., Einaudi, M.T., 1992. Geological characteristics and tectonic setting of proterozoic iron-oxide (Cu-U-Au-Ree) Deposits. Precambr. Res. 58, 241–287.

Hudson, G., 1974. Metallogenesis as related to Crustal Evolution in Southwest Central Peru. University of Liverpool.

Huston, D.L., Sie, S.H., Suter, G.F., Cooke, D.R., Both, R.A., 1995. Trace-elements in sulfide minerals from eastern Australian volcanic-hosted massive sulfide deposits. 1. Proton microprobe analyses of pyrite, chalcopyrite, and sphalerite, and.2. Selenium levels in pyrite – comparison with delta-S-34 values and implications for the source of sulfur in volcanogenic hydrothermal systems. Econ. Geol. Bull. Soc. Econ. Geol. 90, 1167–1196.

Injoque, J., 1985. Geochemistry of the Cu-Fe-Amphibole Skarn Deposits of the Peruvian Central Coast. Unpublished Ph.D. Thesis. University of Nottingham, UK.

Injoque, J., 2002. Fe Oxide-Cu-Au Deposits in Peru: An Integrated View. Hydrothermal Iron Oxide Copper–Gold and related Deposits: A Global Perspective, vol. 2. PGC Publishing, Adelaide, pp. 97–113.

Kajiwara, Y., Krouse, H.R., 1971. Sulfur isotope partitioning in metallic sulfide systems. Can. J. Earth Sci. 8, 1397. http://dx.doi.org/10.1139/e71-129.

Large, R.R., Maslennikon, V.V., Robert, F., Danyushevsky, L.V., Chang, Z.S., 2007. Multistage sedimentary and metamorphic origin of pyrite and gold in the giant Sukhoi Log deposit, Lena gold province, Russia. Econ. Geol. 102, 1233–1267.

Large, R.R., Danyushevsky, L., Hollit, C., Maslennikov, V., Meffre, S., Gilbert, S., Bull, S., Scott, R., Emsbo, P., Thomas, H., Singh, B., Foster, J., 2009. Gold and trace element zonation in pyrite using a laser imaging technique: implications for the timing of gold in orogenic and carlin-style sediment-hosted deposits. Econ. Geol. 104, 635–668.

Li, N., Deng, J., Yang, L.Q., Goldfarb, R.J., Zhang, C., Marsh, E., Lei, S.B., Koenig, A., Lowers, H., 2014. Paragenesis and geochemistry of ore minerals in the epizonal gold deposits of the Yangshan gold belt, West Qinling, China. Miner. Deposita 49, 427–449.

Loewy, S.L., Connelly, J.N., Dalziel, I.W.D., 2004. An orphaned basement block: the Arequipa-Antofalla basement of the central Andean margin of South America. Geol. Soc. Am. Bull. 116, 171–187.

Loftus-Hills, G., Solomon, M., 1967. Cobalt, nickel and selenium in sulphides as indicators of ore genesis. Miner. Deposita 2, 228–242. http://dx.doi.org/10.1007/BF00201918.

Longerich, H.P., Jackson, S.E., Gunther, D., 1996. Laser ablation inductively coupled plasma mass spectrometric transient signal data acquisition and analyte concentration calculation. J. Anal. At. Spectrom. 11, 899–904.

Marschik, R., Fontbote, L., 2001. The Candelaria-Punta del Cobre iron oxide Cu-Au(-Zn-Ag) deposits, Chile. Econ. Geol. Bull. Soc. Econ. Geol. 96, 1799–1826.

Maslennikov, V.V., Maslennikova, S.P., Large, R.R., Danyushevsky, L.V., 2009. Study of trace element zonation in Vent Chimneys from the Silurian Yaman-Kasy volcanic-hosted massive sulfide deposit (Southern Urals, Russia) using laser ablation-inductively coupled plasma mass spectrometry (LA-ICPMS). Econ. Geol. 104, 1111–1141.

McPhie, J., Kamenetsky, V.S., Chambefort, I., Ehrig, K., Green, N., 2011. Origin of the supergiant Olympic Dam Cu-U-Au-Ag deposit, South Australia: was a sedimentary basin involved? Geology 39, 795–798. http://dx.doi.org/10.1130/G31952.1.

Mitchell, R.H., Krouse, H.R., 1975. Sulfur Isotope Geochemistry of Carbonatites. Geochim Cosmochim Acta 39, 1505–1513. http://dx.doi.org/10.1016/0016-7037(75)90152-0.

Molnár, F., Mänttäri, I., O'Brien, H., Lahaye, Y., Pakkanen, L., Johanson, B., Käpyaho, A., Sorjonen-Ward, P., Whitehouse, M., Sakellaris, G., 2016. Boron, sulphur and copper isotope systematics in the orogenic gold deposits of the Archaean Hattu schist belt, eastern Finland. Ore Geol. Rev. 77, 133–162.

Mukasa, S.B., Henry, D.J., 1990. The San Nicolás batholith of coastal Peru: Early Palaeozoic continental arc or continental rift magmatism? Journal of the Geological Society 147, 27–39.

Ohmoto, H., 1972. Systematics of sulfur and carbon isotopes in hydrothermal ore-deposits. Econ. Geol. 67, 551–578.

Ohmoto, H., 1979. Isotopes of Sulfur and Carbon. Geochemistry of Hydrothermal Ore Deposits, pp. 509–567.

Oliver, N.H.S., Cleverley, J.S., Mark, G., Pollard, P.J., Fu, B., Marshall, L.J., Rubenach, M.J., Williams, P.J., Baker, T., 2004. Modeling the role of sodic alteration in the genesis of iron oxide-copper-gold deposits, Eastern Mount Isa block, Australia. Econ. Geol. 99, 1145–1176.

Pollard, P.J., 2006. An intrusion-related origin for Cu-Au mineralization in iron oxide-copper-gold (IOGG) provinces. Miner. Deposita 41, 179–187.

Price, B.J., 1972. Minor Elements in Pyrites from the Smithers Map Area, BC and Exploration Applications of Minor Element Studies. University of British Columbia.

Quang, C.X., 2005. Response of Supergene Processes to Episodic Cenozoic Uplift, Pediment Erosion, and Ignimbrite Eruption in the Porphyry Copper Province of Southern Peru. Econ Geol 100, 87–114.

Rye, R.O., Ohmoto, H., 1974. Sulfur and carbon isotopes and ore genesis – review. Econ. Geol. 69, 826–842.

Scott, R.J., Meffre, S., Woodhead, J., Gilbert, S.E., Berry, R.F., Emsbo, P., 2009. Development of framboidal pyrite during diagenesis, low-grade regional metamorphism, and hydrothermal alteration. Econ. Geol. 104, 1143–1168.

Seal, R.R., 2006. Sulfur isotope geochemistry of sulfide minerals. Sulfide Mineral. Geochem. 61, 633–677. http://dx.doi.org/10.2138/rmg.2006.61.12.

Sillitoe, R.H., 2003. Iron oxide-copper-gold deposits: an Andean view. Miner. Deposita 38, 787–812.

Storey, C.D., Smith, M.P., 2016. Metal source and tectonic setting of iron oxide-copper-gold (IOCG) deposits: evidence from an in situ Nd isotope study of titanite from Norrbotten, Sweden. Ore Geol. Rev.

Thomas, H.V., Large, R.E., Bull, S.W., Maslennikov, V., Berry, R.F., Fraser, R., Froud, S., Moye, R., 2011. Pyrite and pyrrhotite textures and composition in sediments, laminated quartz veins, and reefs at Bendigo Gold Mine, Australia: insights for ore genesis. Econ. Geol. 106, 1–31.

Ushikubo, T., Williford, K.H., Farquhar, J., Johnston, D.T., Van Kranendonk, M.J., Valley, J.W., 2014. Development of in situ sulfur four-isotope analysis with multiple Faraday cup detectors by SIMS and application to pyrite grains in a Paleoproterozoic glaciogenic sandstone. Chem. Geol. 383, 86–99. http://dx.doi.org/10.1016/j.chemgeo.2014.06.006.

Vidal, C.E., Injoqueespinoza, J., Sidder, G.B., Mukasa, S.B., 1990. Amphibolitic Cu-Fe Skarn Deposits in the Central Coast of Peru. Econ Geol Bull Soc Econ Geol 85, 1447–1461.

Wasteneys, H.A., Clark, A.H., Farrar, E., Langridge, R.J., 1995. Grenvillian Granulite-Facies Metamorphism in the Arequipa Massif, Peru – a Laurentia-Gondwana Link. Earth Planet. Sci. Lett. 132, 63–73.

Williams, P.J., Dong, G.Y., Ryan, C.G., Pollard, P.J., Rotherham, J.F., Mernagh, T.P., Chapman, L.H., 2001. Geochemistry of hypersaline fluid inclusions from the Starra (Fe oxide)-Au-Cu deposit, Cloncurry district, Queensland. Econ. Geol. Bull. Soc. Econ. Geol. 96, 875–883.

Zhao, H.X., Frimmel, H.E., Jiang, S.Y., Dai, B.Z., 2011. LA-ICP-MS trace element analysis of pyrite from the Xiaoqinling gold district, China: implications for ore genesis. Ore Geol. Rev. 43, 142–153.

Zhao, X., Zhou, M., Su, Z., Li, X., Chen, W., Li, J., 2017. Geology, geochronology, and geochemistry of the Dahongshan Fe-Cu-(Au-Ag) Deposit, Southwest China: implications for the formation of iron oxide copper-gold deposits in intracratonic rift settings. Econ. Geol. 112, 603–628.

Zhao, X.F., Zhou, M.F., Gao, J.F., Li, X.C., Li, J.W., 2015. In situ Sr isotope analysis of apatite by LA-MC-ICPMS: constraints on the evolution of ore fluids of the Yinachang Fe-Cu-REE deposit, Southwest China. Miner. Deposita 50, 871–884.

Zheng, Y., Zhang, L., Chen, Y.J., Hollings, P., Chen, H.Y., 2013. Metamorphosed Pb-Zn-(Ag) ores of the Keketale VMS deposit, NW China: evidence from ore textures, fluid inclusions, geochronology and pyrite compositions. Ore Geol. Rev. 54, 167–180.